The fractal turbulent/non-turbulent interface in the atmosphere

Lars Neuhaus, Matthias Wächter, and Joachim Peinke

ForWind - Institute of Physics, University of Oldenburg, Küpkersweg 70, 26129 Oldenburg, Germany

Correspondence: lars.neuhaus@uol.de

Abstract. With their steady growth in size, wind turbines are reaching unprecedented heights. As a result, at these heights they are affected by wind conditions that have not yet been investigated in detail. With increasing heights, a transition to laminar conditions becomes more likely. In this paper, the presence of the turbulent/non-turbulent interface (TNTI) in the atmosphere is studied. Three different sites are investigated. Our fractal scaling analysis leads to typical values known from ideal laboratory and numerical investigations. The height distribution of the probability of the TNTI is determined and shows a frequent occurrence at the height of the rotor of future multi megawatt turbines. The indicated universality of the fractality of the TNTI allows the use of simplified models in laboratory and numerical investigations.

1 Introduction

Wind turbines are getting bigger, reaching heights above 250 m, and are installed farther offshore. The turbulent wind at those locations and heights is rarely measured. Hence, the environmental conditions for future offshore wind turbines are still sparsely studied. However, those conditions have significant influence on the performance of wind turbines. Wind fluctuations on short time scales are known to induce fluctuations in the power output of wind turbines (Milan et al., 2013). Further, also a varying turbulence intensity (TI) of the inflow over the rotor is significantly influencing the turbine operation (Lobo et al., 2023).

For the new developments in wind energy, the transitions from turbulent to laminar conditions become more relevant. In particular the complexity of these turbulent/non-turbulent interfaces (TNTI) may effect the working conditions, what is the focus of our paper.

While the TNTI is extensively studied in laboratory flows, it is hardly investigated in the atmosphere. Available data covers heights up to 100 m offshore by met mast measurements as by the FINO platforms and up to 200 m onshore as by the met mast at Cabauw. Extremer heights up to 250 m offshore are measured by Lidar systems, which however provide lower temporal resolution. Recently, flights were undertaken to investigate the turbulence around wind parks, covering different heights (Lampert et al., 2020). However, flights allow only for a short observation period and may give only a limited picture regarding turbulent properties.

The question is, if we can find similarities between the features of TNTI of ideal laboratory and numerical investigations and those of atmospheric situations. The objective of this paper is to perform an initial characterization of atmospheric data to detect the TNTI in the atmosphere and compare it based on known features, namely fractal characteristics. Thus, the purpose

is not to discuss minor details, but to give a basic idea of the presence of the TNTI in the atmosphere and of the possibilities to characterize it.

The applied method is described in detail for measurements at the FINO1 platform and additional sites are investigated to provide a more complete picture. The measurement sites considered are described in Sect. 2. The basic features and methods of characterization of the TNTI are presented in Sect. 3. The results of the analysis are presented in Sect. 4 and discussed in Sect. 5. Sect. 6 concludes this paper.

2 Measurement sites

For the analysis three different sites with height resolved data are analysed. The FINO1 met mast, the Cabauw met mast (Lidar measurments available), and Lidar measurements at the offshore platform Borssele Alpha are considered.

The FINO1 offshore met mast has a height of 103m (FINO1, 2023). It is selected for a detailed discussion, as it is a well known offshore platform, which provides temporal high resolved data on a long observation period. Cup anemometer at $33\,\mathrm{m}$, $40\,\mathrm{m}$, $50\,\mathrm{m}$, $60\,\mathrm{m}$, $70\,\mathrm{m}$, $80\,\mathrm{m}$, $90\,\mathrm{m}$, and $100\,\mathrm{m}$ record the wind speed with a sampling frequency of 1Hz. Wind vanes at 33m and 90m record the wind direction. As for certain inflow directions the mast influences the measurements, data for wind directions between 275° and 350° of either directional sensor are neglected (filled with NaNs) to ensure undisturbed inflow. Further, as FINO1 is located next to several wind parks, only data up to the date of the assembly of the first wind turbine are considered. The available time period is hence from 01.01.2007 to 15.07.2009. Further, low wind speeds ($u < 0.5\,\mathrm{m\,s^{-1}}$), which tend to unreasonable high TI and which have minor importance for the operation of wind turbines, are neglected (data filled with NaNs).

The Cabauw wind data were made available by the Royal Netherlands Meteological Institute (KNMI) (Hansen et al., 2021). The $213\,\mathrm{m}$ high met mast is installed onshore. Propeller anemometer at $20\,\mathrm{m}$, $40\,\mathrm{m}$, $80\,\mathrm{m}$, $140\,\mathrm{m}$, and $200\,\mathrm{m}$ record the wind speed with a sampling frequency of 2Hz. For the time period from 1985 to 1986 roughly 480 hours are available.

At the same site Lidar measurements were conducted and made available by KNMI (KNMI, 2023a, b). Two data sets recorded by a ZephIR 300M wind lidar are avaibale. One data set (Cabauw Lidar ZP) includes wind speeds at seven heights from $10\,\mathrm{m}$ to $251\,\mathrm{m}$ (not equidistant) with a temporal resolution of about $11\,\mathrm{s}$. This data is available in the time period from 15.02.2018 to 07.06.2020. The second data set (Cabauw Lidar ZX) includes wind speeds at eleven heights from 10m to 299m (not equidistant) with a temporal resolution between $17\,\mathrm{s}$ and $18\,\mathrm{s}$. This data is available in the time period from 20.02.2020 to 07.06.2020.

Further, data by Lidar measurements at the Borssele Alpha offshore platform (BSA) next to the wind park Borssele I-V (operation started in September 2021) is used which was also made available by KNMI (KNMI, 2023c). Data was recorded by a ZephIR 300M wind lidar at 11 heights from $14\,\mathrm{m}$ to $249\,\mathrm{m}$ (not equidistant) with a temporal resolution between $17\,\mathrm{s}$ and $18\,\mathrm{s}$. Data is available from end of 2019 until now. Measurements are still ongoing. The considered time period in this paper is from 21.11.2019 to 31.08.2021.

3 Method

60 In this section, the approach used in this work to detect and to characterize the TNTI is presented. A brief introduction to laboratory experiments on the TNTI is given (Sect. 3.1). Section 3.2 describes the characterization of boundaries based on the fractal dimension. In Sect. 3.3, a method for characterizing the TNTI in the atmosphere based on one-point measurements of the wind velocity is given and shown exemplarily for the FINO1 site.

3.1 Turbulent/non-turbulent interface (TNTI)

65 Between different flow states, as turbulent and non-turbulent, an interfaces forms. An example of a turbulent/non-turbulent interface (TNTI) of a jet is shown in Fig. 1. Mixing of the two flow phases occur on large and small scales. It can be recognized how the complexity of this interface increases downstream.
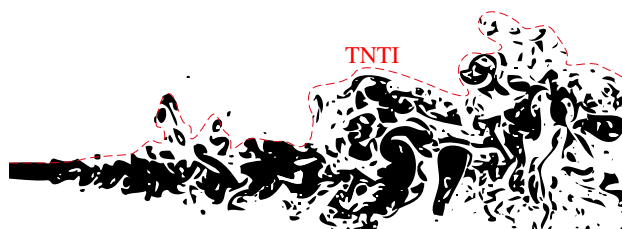
Figure 1. Jet flow visualized by laser induced fluorescence (adapted from Dimotakis et al. (1981); Sreenivasan and Meneveau (1986)). The fractal boundary between the turbulent flow and the laminar surrounding can be seen. It is here indicated by a red line, which is an approximation of the TNTI.

The TNTI was first investigated by Corrsin and Kistler (1955) in laboratory flows. Sreenivasan and Meneveau (1986) first described the boundary between laminar and turbulent flows by its fractal dimension. They studied a developing turbulent

70 boundary layer on a flat plate. The turbulent flow was visualized by smoke. Images were recorded, and a brightness threshold was used to determine the TNTI. By changing the resolution of the images different scales were resolved and a fractal dimension of the TNTI of roughly 2.4 between Kolmogorov length scale and $1/6$ integral length scale L was found. For a reduction of the TNTI to a two dimensional plane of observation the fractal dimension reduces to 1.4 and in a one dimensional case 0.4.

Following this work more detailed studies with more sophisticated methods, as particle image velocimetry (PIV), were

75 undertaken. de Silva et al. (2013) used PIV measurements to detect the TNTI in a boundary layer flow by a threshold of the turbulent kinetic energy (TKE). They found a more precise fractal dimension of 2.36 on scales of 20% L towards smallest scales (limited by resolution). Based on these results we define a fractal dimension of a TNTI of 2.36 (or 0.36 from a 1-dimensional cut, as explained below) as a typical TNTI fractal dimension.

While the TNTI itself is rather thin its position is strongly varying. The TNTI is formed on large scales by engulfment (large

80 scale fluctuations of the interface) and on small scales by nibbling (viscous diffusion process). From large to small scales the

TNTI exhibits a self similarity, which can be found in the fractal dimension. A detailed review on the TNTI is given by da Silva et al. (2014) and more recent summary is given by Xu et al. (2023).

3.2 Fractal dimension

This turbulent/non-turbulent interface is commonly described by its fractal characteristics. Fractals were intensively studied by Mandelbrot (1982) and became an object of interest for the scientific community. To characterize a fractal its fractal dimension can be used.

An exemplary fractal curve, which corresponds to a boundary in two-dimensional space, is given by a Koch curve (Fig. 2). The scheme of construction is that from an interval the center subinterval is replaced by two subintervals of the same size. From the resulting intervals, the center subintervals are again replaced by two subintervals of the same size, and so on to smaller and smaller intervals (increasing order n). The result is a fractal boundary, which in this case is following a strict geometric law.

The fractality, the fractal dimension, of this Koch curve can be estimated by a box counting approach. To do so, boxes with different edge length r are used and the amount of boxes $N(r)$ which are needed to cover the curve are counted. The fractal dimension D_f can then determined by the slope of the relation

$$N(r) \propto r^{-D_f} \tag{1}$$

to 1.262 for the Koch curve (Sreenivasan and Meneveau, 1986).

In real-world applications, not always spatially high resolved data is available. Especially atmospheric data is mostly only available by point wise measurements. By Taylor's hypothesis of frozen turbulence (Taylor, 1938) this will give a one-dimensional slice through a three dimensional field. However, by the additive rule of co-dimensions for intersecting sets

$$D_{f,3} = D_{f,2} + 1 = D_{f,1} + 2 \tag{2}$$

the fractal dimension $D_{f,d}$ in higher embedding dimensions d can be estimated by data collected in a lower embedding dimensions (Mandelbrot, 1982; Sreenivasan and Meneveau, 1986).
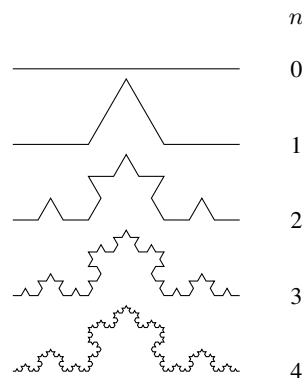
Figure 2. Koch curve of the order n.
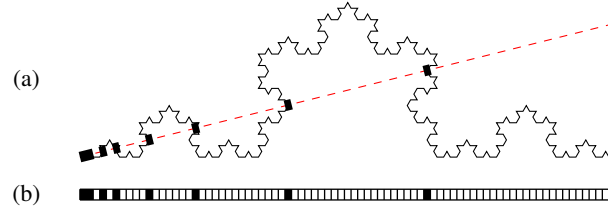
Figure 3. Koch curve f order 4 with one-dimensional slice and marked intervals of crossings with the Koch curve (a). The corresponding intervals give the Cantor set like plot (b).

Thereby, a simple way to estimate the fractal characteristic of a boundary in three-dimensional or two-dimensional space is to consider a one-dimensional slice (e.g. a single point measurement of the wind speed). This slice (red dashed line in Fig. 3 (a)) is covered with intervals of size r and intervals with and without a crossing of the boundary are obtained (as indicated in Fig. 3 (b)). The fractal dimension of this slice can be estimated after Eq. 1 by the number of intervals $N(r)$ on the scale r needed to cover the boundary crossings. The result of this box counting approach is $D_{f,1} = 0.262$ and after Eq. 2 gives the correct $D_{f,2} = 1.262$.

From this it becomes clear, that the fractal dimension of higher dimensional fractals can be estimated from a one-dimensional slice. Consequently, an adequate estimate of the fractality of the TNTI in the atmosphere can be made by the available single point measurements, which correspond to a slice through a three-dimensional wind field.

3.3 Applied method

Typically, when applying methods to calculate the fractal dimension, the challenge lies in determining the interface using a threshold. Details on the herein applied method are discussed for the FINO1 site. A similar procedure as in de Silva et al. (2013) is used to estimate the TNTI. To determine the TNTI, the instantaneous turbulent kinetic energy (TKE) is used to detect transitions between laminar and turbulent phase. Subsequently, the just mentioned box counting approach is applied to characterize the TNTI by its fractality.

The instantaneous TKE is approximated by

$$E = \frac{1}{2}(u - u_{\text{movavg}})^2 \tag{3}$$

with the moving averaged wind speed

$$u_{\text{movavg}} = \frac{1}{T f_s} \sum_{\Delta t = -T/2}^{T/2} u(t + \Delta t). \tag{4}$$

Here the sampling frequency f_s and the filter span T of $20\,\text{s}$ (for cup and propeller anemometer) and $90\,\text{s}$ (for Lidar measurements) are used.

For better comparison of different mean wind speeds, the instantaneous TKE is normalized

$$E_{\text{norm}} = E/u_{\text{movavg}}^2 \tag{5}$$
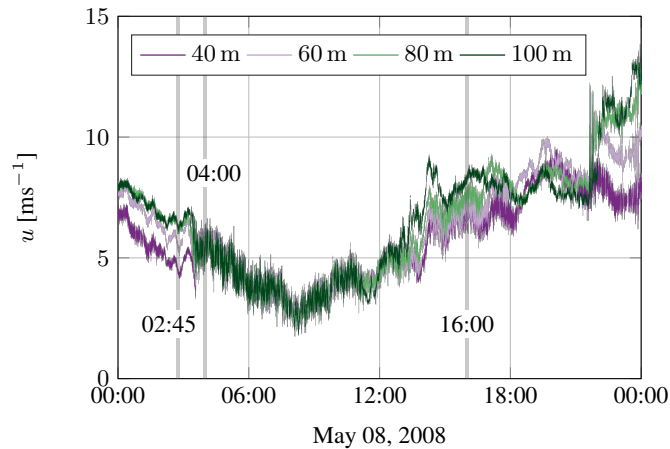
Figure 4. Exemplary velocity time series at FINO1 on May 08, 2008 for different heights. Vertical gray bars indicate exemplary 10 minute sections shown in Fig. 5 and Fig. 6.

125 by the square of the moving averaged wind speed. The threshold between turbulent and non-turbulent phase is set to 0.001, which is in the order of the threshold used by de Silva et al. (2013). Data points where this threshold is crossed will be referred to as crossings in the following.

The next steps are shown examplarily for a day (May 8, 2008) of the FINO1 data set (Fig. 4), as this day exhibits many laminar periods. The investigation is done for sections of 10 minute length. In Fig. 5 crossings of the TNTI are visualized for
130 the different heights.

Figure 5 (a) shows the behavior of a rather turbulent 10 minute section. Plenty crossings can be observed at different heights. This is not always the case as shown by the selected section of Fig. 5 (b) and (c). In Fig. 5 (b) a laminar phase at high altitudes (100 m) with no crossings is shown whereas at lower altitudes crossings can be recognized. Figure 5 (c) shows the behavior of a section with laminar flow at all altitudes. Almost no crossings of the threshold occur.

135 To estimate the fractal dimension (Eq. 1), our box counting approach is applied for every individual 10 minute section for each height. Boxes of a certain size r_{Box} (respectively duration T_{Box}) are used. Taylor's assumption of frozen turbulence $r_{\text{Box}} = \langle u \rangle T_{\text{Box}}$ is used to change the time dependence into a spatial scale dependency (Taylor, 1938).

Next, the number of boxes with at least one crossing of the threshold is counted. After Eq. 1 the resulting number of counted boxes N_{Box} over box size r_{Box} is plotted in a double logarithmic presentation (Fig. 6). To improve the quality of the estimated
140 slope, boxes are overlapping 90%.

It can be recognized, that mainly three different slopes can be found. A slope of -1 is found for fully turbulent behavior as shown in Fig. 6 (a). A slope of -0.36 was found for sections with turbulent and laminar phases (Fig. 6 (b)). For sections with mostly laminar flow, the slope is close to 0 (Fig. 6 (c)). Note the scaling ranges for different exponents not always extend over the whole range, but are often limited only to some sub ranges of the scales as seen in Fig. 6 (a,b).
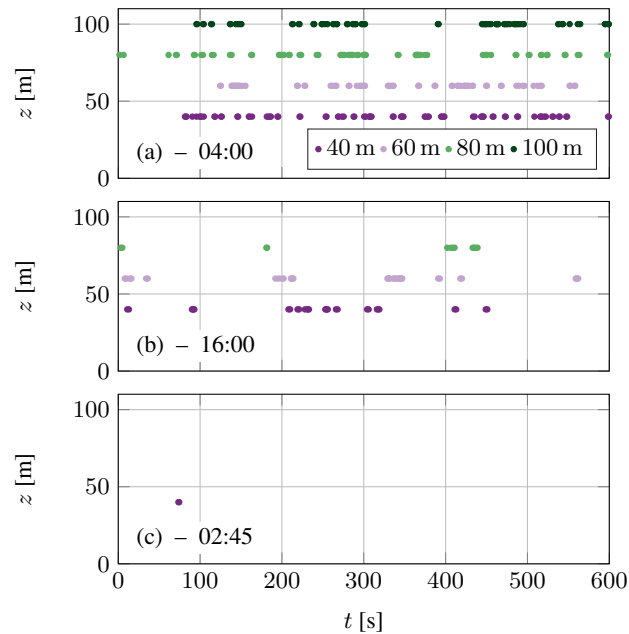
Figure 5. Crossings indicating the transition between laminar and turbulent phase for an exemplary turbulent (May 08, 2008 04:00) (a), turbulent/non-turbulent (May 08, 2008 16:00) (b) and laminar (May 08, 2008 02:45) (c) section. A Cantor set like plot as shown in Fig.3 (b).

The fractal dimension is determined by the negative slope of the just discussed presentation. The selection of the sub range of scales is motivated by our wind energy application. We take scales from roughly 3 m to 250 m corresponding to the order of a wind turbine chord length and rotor diameter, respectively.

Not for all 10 minute sections a clear slope is obtained. Sometimes a super position of different slopes is found. For our purpose here, we take such events as ranges with no self-similarity (constant slope). To do so, 10 minute sections exhibiting residual standard errors S_r of the slope larger than 0.02 are neglected (NaN). By this only sections with a constant fractality over roughly two decades are considered. For the exemplary day (May 08, 2008) the resulting time series of the fractal dimension D_f are shown in Fig. 7. The values for the three exemplary times (04:00, 16:00, and 02:45) are given in Table 1.

4 Results

The analysis of the measurement sites is done in three steps. First a basic analysis of the turbulence intensity at the different sites and heights is done (Sect. 4.1). In the following the presence of a typical TNTI fractal dimension is investigated (Sect. 4.2). Last, the likelihood of the presence of the TNTI and its fractal dimension at certain heights is investigated for all sites (Sect. 4.3).
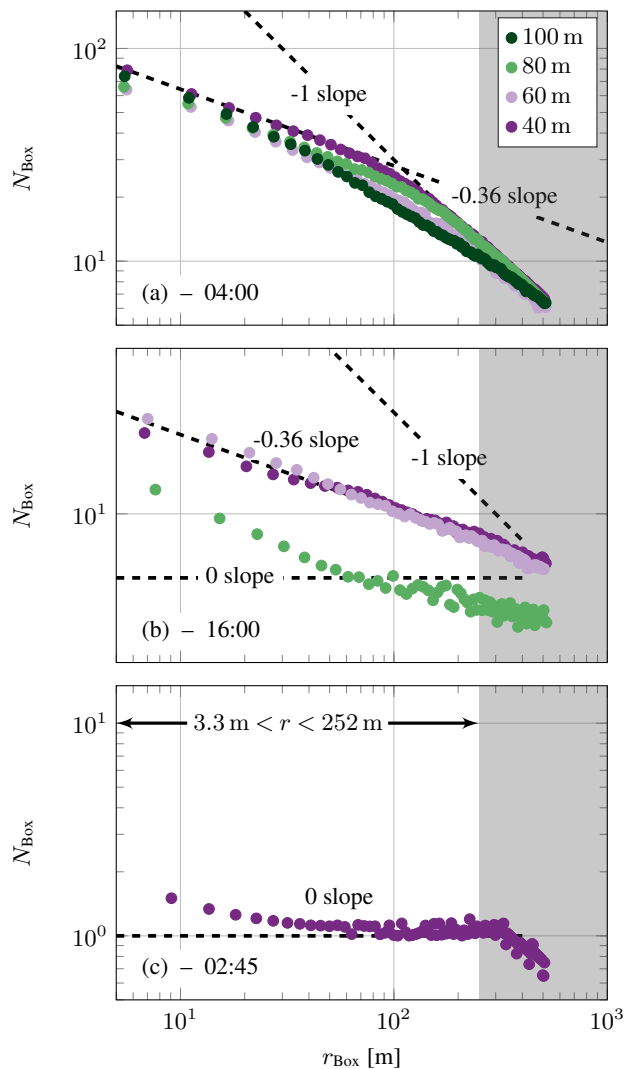
Figure 6. Number of boxes containing at least one threshold crossings N_{Box} as a function of the box size for three 10 minute sections around May 08, 2008 04:00 (turbulent) (a), May 08, 2008 16:00 (TNTI) (b), and May 08, 2008 02:45 (laminar) (c), according to Fig. 5.
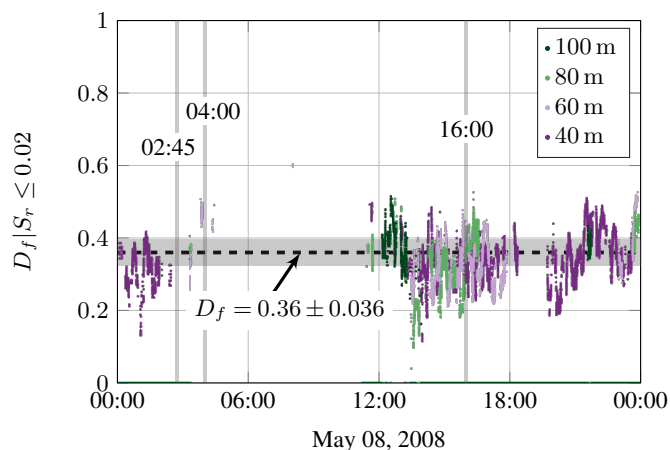
Figure 7. Estimated fractal dimension D_f on May 08, 2008. Only results are shown when a reasonable fractal dimensions could be determined. Different colors stand for different heights. The dashed line indicates the typical TNTI fractal dimension of 0.36 and the shaded gray area a range of ± 0.036 around this value. Vertical gray bars indicate exemplary 10 minutes section shown in Fig. 5 and Fig. 6.

Table 1. Fractal dimension D_f and residual standard error S_r on May 08, 2008 at different times and for different heights. Valid entries ($S_r \leq 0.02$) are shown in a **bold** font and neglected entries ($S_r > 0.02$ or NaN) are shown in an *italic* font.

Time	z [m]	D_f	S_r
	100	*0.5246*	*0.0328*
	80	*0.4297*	*0.0407*
04:00 – Fig. 5 (a) & Fig. 6 (a)	*60*	*0.4774*	*0.0409*
	40	*0.4653*	*0.0460*
	100	*NaN*	*NaN*
	80	*0.3912*	*0.0350*
16:00 – Fig. 5 (b) & Fig. 6 (b)	**60**	**0.3780**	**0.0096**
	40	**0.3063**	**0.0127**
	100	*NaN*	*NaN*
	80	*NaN*	*NaN*
02:45 – Fig. 5 (c) & Fig. 6 (c)	*60*	*NaN*	*NaN*
	40	*NaN*	*NaN*

4.1 Turbulence intensity

The turbulence intensity

$$\text{TI} = \sigma(u_{\text{detrend}})/\langle u \rangle \tag{6}$$

160 is calculated by the standard deviation σ. u_{detrend} denotes the velocity timeseries detrended by a linear fit, and $\langle u \rangle$ denotes the mean wind speed for a section of 10 minute length. Only 10 minute sections with at least 75% valid data are considered.

Figure 8 shows the resulting probability density functions (PDF) for the individual sites. All sites show an increase of low turbulence intensity events with height. For $TI < 1\%$ the results seem to get physical unreasonable. Here also strong influences of the measurement techniques are expected. However, this is not of relevance for the analysis in this paper and
165 hence not further discussed.

The overall trend to lower TI at higher heights is further visualized by a decrease of the median of the TI (med(TI)) as a function of z (see Fig. 9). The measurements at FINO1 revealed the lowest median TI. Compared to the two offshore sites (FINO1 and Borssele), the measurements at the onshore site Cabauw show a significant higher TI at lower altitudes. The lidar measurements (Cabauw Lidar ZP, Cabauw Lidar ZX, and Borssele) show comparable curves. However, a direct comparison is
170 difficult due to the different measurement methods.

4.2 Fractal dimension of the TNTI

Next the fractal dimension of the TNTI is investigated for 10 minute section with an overlap of $9\,\text{min}$. Figure 10 shows the individual probability density function (PDF) of the fractal dimension D_f for different TI ranges.

As shown in Fig. 10 (a), for a low TI ($< 2.5\%$), most found fractal dimensions are smaller than the expected typical TNTI
175 fractal dimension of 0.36 (see Sect. 3.1). This is in accordance with Fig. 6, as laminar phases tend to exhibit a slope closer to 0.

For medium TI ($2.5\% < \text{TI} < 7.5\%$), significantly more valid fractal dimensions are found. As seen in Fig. 10 (b), the found values match well with the expected value of 0.36. Further, a clear height dependence can be found with more 10 minute sections with a typical TNTI fractal dimensions at higher altitudes.

For high TI ($< 7.5\%$) only few valid fractal dimensions are found, see Fig. 10 (c). One peak in the PDF can be recognized at
180 values slightly above the typical TNTI fractal dimension and one even smaller peak close to 1. Again in good agreement with Fig. 6, as turbulent sections tend to exhibit slopes closer to 1.

In Fig. 11 different probabilities of sections with a fractal dimension $D_f = 0.36$ within a $\pm 10\%$ range are shown. These probabilities are conditioned on the 10 minute section TI (Fig. 11 (a)), the mean wind speed $\langle u \rangle$ (Fig. 11 (b)), and the shear exponent α (Fig. 11 (c)).

185 For periods with low TI ($< 2.5\%$) and high TI ($> 7.5\%$) only few events with a typical TNTI fractal dimension can be recognized (Fig. 11 (a)). For sections with TIs in between ($2.5\% < \text{TI} < 7.5\%$), it is more likely to exhibit both (laminar and turbulent) phases. Up to 17% of these observed 10 minute sections showed a typical TNTI fractal dimension.

At low mean wind speeds the percentage of sections with typical TNTI fractal dimension is rather indifferent over height (Fig. 11 (b)). This changes with increasing mean wind speed. A typical TNTI fractal dimension becomes more likely at higher
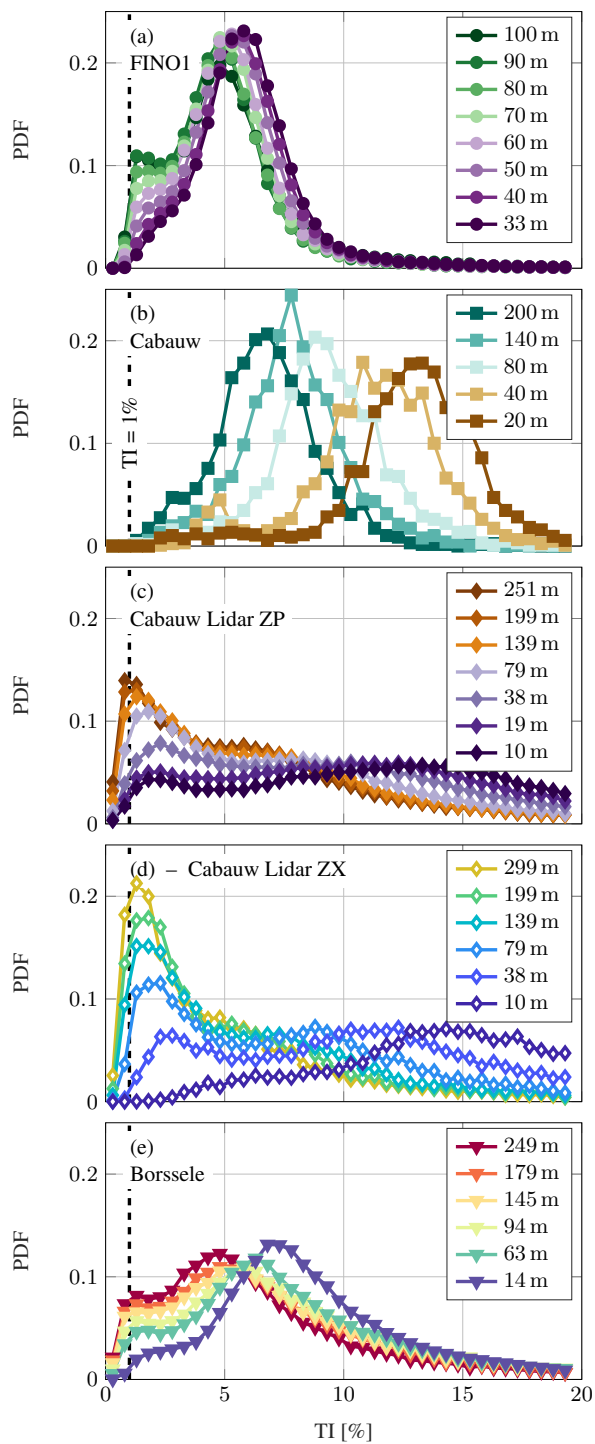
Figure 8. Probability density functions (PDF) of the turbulence intensity at different heights for the data sets FINO1 (a), Cabauw (b), Cabauw Lidar ZP (c), Cabauw Lidar ZX (d), and Borssele (e).
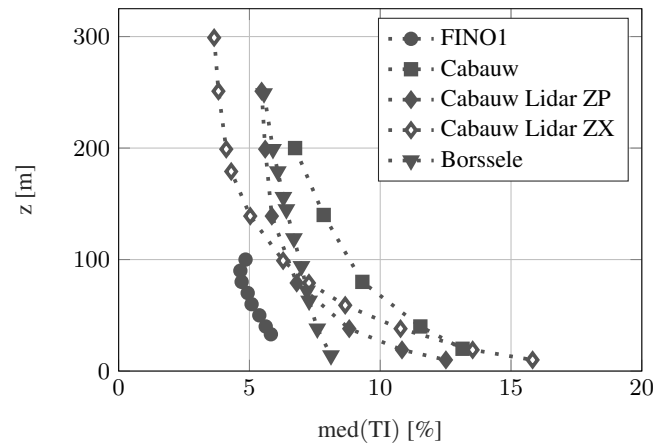
Figure 9. Median of the turbulence at different heights and for the different data sets.

altitudes and less likely at lower altitudes. However, for high mean wind speeds ($> 15\,\mathrm{m\,s^{-1}}$) the probability for a typical TNTI fractal dimension is reduced at all heights.

Figure 11 (c) shows results from data set conditioned on the shear exponent α. α is estimated for all 10 minute sections by fitting the power law formulation $u(z) = u(z_{\mathrm{ref}}) \left(\frac{z}{z_{\mathrm{ref}}} \right)^{\alpha}$ were z_{ref} is given by the highest altitude. Again, the probability of a typical TNTI fractal dimension becomes more likely with height. With increasing shear the probability of a typical TNTI fractal dimension has a maximum at altitudes around 60 m and decreases at higher altitudes. For extreme shear ($\alpha > 0.3$), the likelihood of a typical TNTI fractal dimension at higher altitudes (<90 m) is reduced by half compared to lower shear ($\alpha < 0.3$).

Overall these probability investigations show that the occurrence of typical TNTI fractal dimensions are not negligible, but often are higher then 10% of the data.

4.3 Universality

Next an overview of results from all data sets is given. For the lidar measurements the estimation of the fractal dimension is adapted due to the lower sampling rate. The 10 minute sections is extended to 90 minute sections and the fractal dimension is estimated for scales from $200\,\mathrm{m}$ to $2.5\,\mathrm{km}$. Thus, the lidar measurements are used to investigate the presence of the TNTI on larger scales.

Figure 12 shows the distribution of the fractal dimension for the individual data sets, according to Fig. 10 (b) for $2.5\% < \mathrm{TI} <$ 7.5%. An accumulation of the fractal dimension for all data sets can be found. However, some deviations can be recognized. At lower heights a stronger deviation towards larger or smaller fractal dimensions can be recognized for the lidar measurements (Fig. 12 (c-e)). For more extreme heights, the fractal dimension tends to be closer to the typical TNTI fractal dimension of 0.36. However, a broader distribution and shifts towards higher and lower fractal dimensions can be observed.

The propeller measurements at Cabauw show only few events with a slightly towards lower values shifted fractal dimensions (Fig. 12 (b)). The results at 20m are questionable and might be effected by ground structures.
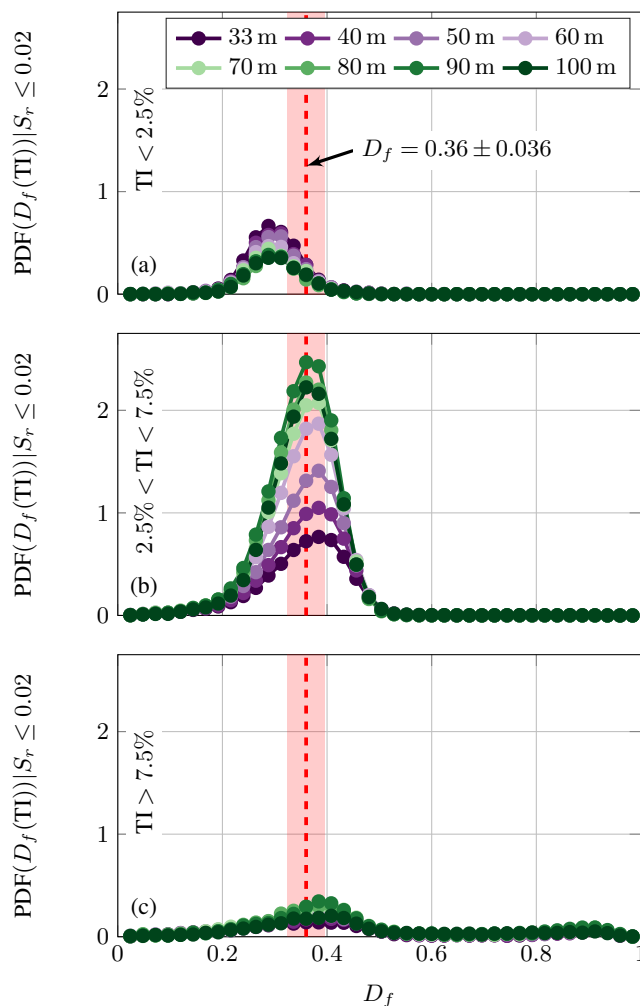
Figure 10. Probability density function of the fractal dimension D_f conditioned on the different TI ranges: TI $< 2.5\%$ (a), $2.5\% <$ TI $< 7.5\%$ (b), and TI $> 7.5\%$ (c). The red dashed line indicates the typical TNTI fractal dimension of 0.36 and the shaded red area a range of ± 0.036 around this value. The normalization of the PDFs is done based on all sections including invalid fractal dimensions ($S_r \leq 0.2$), which are not shown but would correspond to a peak at "NaN".
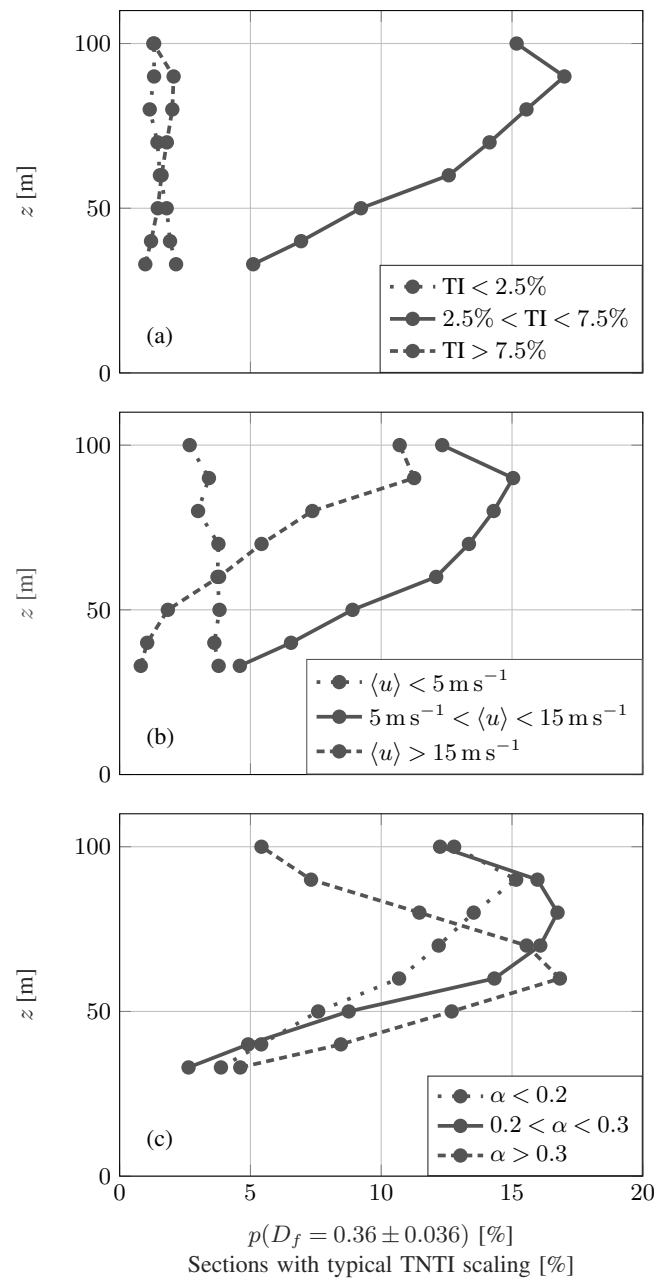
Figure 11. Percentage of data exhibiting a typical TNTI fractal dimension conditioned on different TI level (a), mean wind speeds (b), and shear (c).

In contrast to the other data sets, the best values for the Cabauw Lidar ZP are obtained for 10m with 0.2 ± 0.1 (Fig. 12 (c)). The peak of the fractal dimension gets more smeared out as the heights increase.

The results from Cabauw Lidar ZX show a consistent trend from which only the low altitude deviates (Fig. 12 (d)). With increasing height the peak of the fractal dimension becomes narrower and is shifted towards lower fractal dimensions from 215 0.56 at 38m to 0.43 at 299m.

Also the results from Borssele show a consistent picture with clearer and more frequent fractal structures at higher altitudes (Fig. 12 (e)). However, the fractal dimension peak is at 0.46 and hence higher than the expected typical TNTI fractal dimension of 0.36.

For all sites and data sets it can be recognized, that the probability of the typical TNTI fractal dimension ($0.324 \geq D_f \leq$ 220 0.396) increases with height (Fig. 13). The obtained probabilities depend on sites and measurement methods. The FINO1 data set shows the highest ratio of typical TNTI fractal dimension. For the Cabauw site the dependence on different measurement methods or, respectively, time resolution of the measurements, is seen.

5 Discussion

A frequent presence of the turbulent/non-turbulent interface (TNTI) in the atmospheric data is observed. A clear accumulation 225 of the fractal dimension of this TNTI around 0.36 is found, for the most reliable data set FINO1 with a high temporal resolution and a long observation period. To our interpretation this is in astonishing good agreement with experiments in the laboratory (see de Silva et al. (2013)).

If investigating the individual sections of a data set, fractality (self similarity) on different scales can be observed. The box counting approach showed mainly three different slopes, 1 for fully turbulent flow, 0.36 for the TNTI, and 0 for fully 230 laminar flow (Fig. 6). The slopes are not necessary constant on different scales. Different slopes on different scale ranges can be present (see also Sreenivasan and Meneveau (1986)). When conditioning on the fit quality by the residual standard error, mostly the typical TNTI fractal dimension of 0.36 is observed (Fig. 10). By this approach only fractal dimensions with a constant fractality over the investigated scales (two decades) are considered. If the fractality changes over the investigated scales, the fractal dimensions are neglected. Hence, if a partially typical TNTI fractal dimension would be considered, even 235 higher amounts of sections with a typical TNTI fractal dimension might be found.

As a side remark, we would like to point out that an increased probability of fractal dimensions in the order of 2/3 is observed in the lidar measurements at low altitudes (see Fig. 12 (c-e)). This could be interpreted as a consequence of thermally driven (convective) flow fields exhibiting a 2/3 scaling (Grossmann and Lohse, 1994).

Differences are observed at different measurement locations and for different measurement techniques, including temporal 240 resolution, spatial resolution, and observed periods. The resolution of the measurement is important to get proper values. In Fig. 11, reduced probabilities are observed at 100m, which do not follow the trends. This phenomenon, that the statistics of the measurement point at 100m deviate from those at the other heights, is known but unexplained for the FINO1 data set.
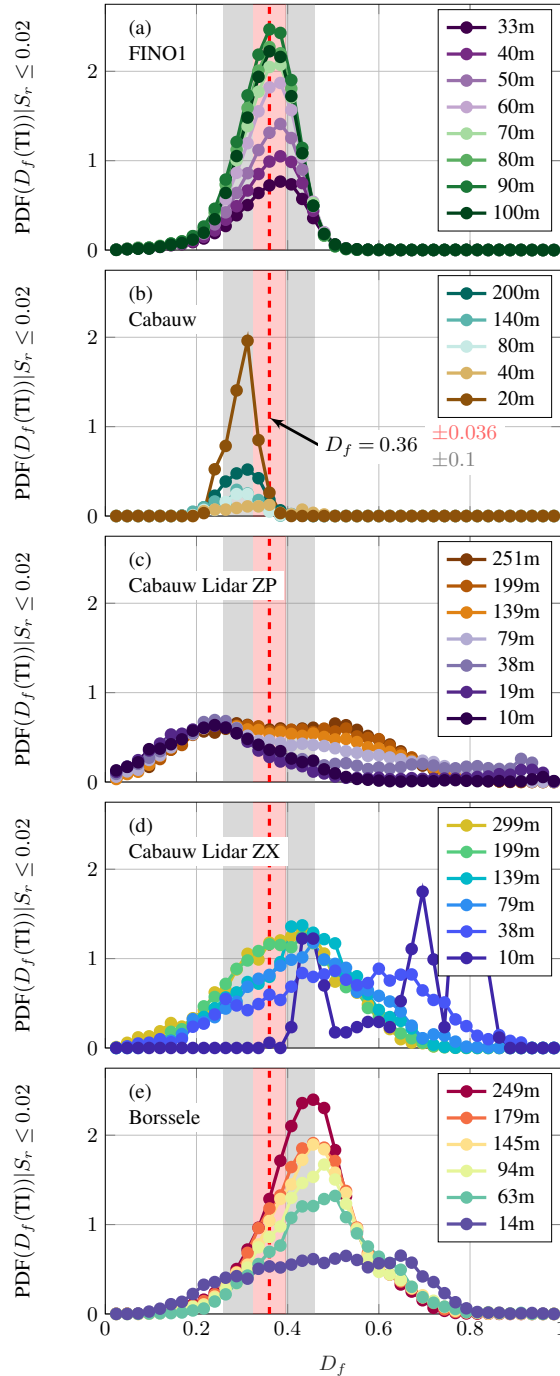
Figure 12. Probability density function (normalization according to Fig. 10) of the fractal dimension D_f conditioned on the TI range $2.5\% < \text{TI} < 7.5\%$ for FINO1 (a), Cabauw (b), Cabauw Lidar ZP (c), Cabauw Lidar ZX (d), and Borssele (e). The red dashed line indicates the typical TNTI fractal dimension of 0.36 and the shaded red area a range of ± 0.036 (gray area ± 0.1) around this value.
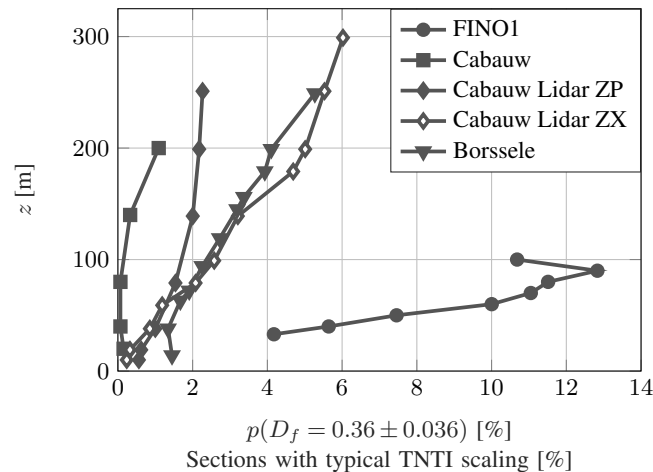
Figure 13. Percentage of data exhibiting a typical TNTI fractal dimension.

At higher altitudes more fractal subsets are seen. This is expected, as in the meteorological context the TNTI can be understood as the dynamic interface between the turbulent atmospheric boundary layer (commonly known as the Prandtl layer) and the laminar flow (which could be referred to as laminar Ekman layer) that occurs at higher altitudes. The estimated fractal dimension of the TNTI accumulates around a specific value for all data sets - which is in a first order approximation close to 0.36, the reference value of ideal lab experiments. Lidar measurements, which cover different (larger) scales, also show an accumulation of the fractal dimension at a certain value, suggesting a universal meaning of the fractality of the TNTI. However, deviations (± 0.1) of the fractal dimension are found, which might be due to effects coming from different orography and measuring techniques and need to be further investigated.

6 Conclusions

The presence of the turbulent/non-turbulent interface (TNTI) in the atmosphere at different sites has been studied. Our results of fractal dimension of 0.36 ± 0.1 we take as strong hint for comparable trends for the different measurements sites.

The fractal dimension, a simple multi-scale approach, provides an effective method for characterizing the complexity of the TNTI. The from laboratory experiments known typical TNTI fractal dimension of 0.36 of the TNTI is quite close to the values found in the atmosphere. The highest likelihood for a typical TNTI fractal dimension is found at high altitudes. Hence, the geometry of the TNTI for atmospheric cases and more ideal flow situations in laboratory experiments and numerical simulations seem to be quite similar. This opens new possibilities for further detailed studies.

Independent of the measurement location and procedure, a significant amount of sections with a typical TNTI fractal dimension is detected. Our analysis of several data sets reveals that the fractality of the TNTI occurs at very different scales, from the size of a wind turbine blade to several kilometers (as seen in lidar data). Up to more than 10% of the observed time a TNTI

at small (for a wind turbine relevant) scales is present at heights above 60 m (offshore, FINO1). This hints on a very frequent presence of the TNTI at altitudes of a multi megawatt wind turbine rotor.

Further and more detailed investigations need to be made to get a complete picture of the TNTI in the atmosphere. High
265 spatial and temporal resolved data over long periods are needed to gain further knowledge on its small scale behavior.

These findings make the consideration of laminar flows and the frequent presence of the TNTI at higher altitudes relevant for wind turbine research. This becomes particularly important for large offshore wind turbines in the multi megawatt class. The sudden jump between two significantly different turbulence states could cause additional load cycles for the turbine components. Experimental and numerical studies are needed to investigate the effects of the TNTI on wind turbines and to clarify
270 whether the TNTI needs to be considered in turbine design and operation. For this an indicated universal structure of the TNTI is very helpful.

Data availability. Wind data for the Cabauw and Borssele site were made available by the Royal Netherlands Meteological Institute (KNMI)

Author contributions. LN analyzed the data and wrote the manuscript draft. MW and JP supervised the work and reviewed and edited the manuscript.

275 *Competing interests.* At least one of the (co-)authors is a member of the editorial board of *Wind Energy Science*.

Acknowledgements. We acknowledge helpful discussions with Michael Hölling, Fabien Thiesset and Jan Friedrich. The project has been funded by the Deutsche Forschungsgemeinsschaft (DFG, German Research Foundation) – SFB1463 – 434502799.

References

Corrsin, S. and Kistler, A. L.: Free-stream boundaries of turbulent flows, Tech. rep., JOHNS HOPKINS UNIV BALTIMORE MD, 1955.

280 da Silva, C. B., Hunt, J. C., Eames, I., and Westerweel, J.: Interfacial layers between regions of different turbulence intensity, Annu. Rev. Fluid Mech, 46, 567–590, 2014.

de Silva, C. M., Philip, J., Chauhan, K., Meneveau, C., and Marusic, I.: Multiscale geometry and scaling of the turbulent-nonturbulent interface in high Reynolds number boundary layers, Physical review letters, 111, 044 501, 2013.

Dimotakis, P., Lye, R., and Papantoniou, D.: In 15th Intl Symp, Fluid Dyn., Jachranka, Poland, 1981.

285 FINO1: FINO1, Forschungsplattformen in Nord- und Ostsee, https://www.fino1.de/en/ (accessed: 05.01.2023), 2023.

Grossmann, S. and Lohse, D.: Fractal-dimension crossovers in turbulent passive scalar signals, Europhysics letters, 27, 347, 1994.

Hansen, K. S., Vasiljevic, N., and Sørensen, S. A.: Wind data from the tall Cabauw met mast, https://doi.org/10.11583/DTU.14153192.v1, 2021.

KNMI: Wind - lidar data from ZephIR 300M (unit ZX973) during Cabauw campaign 2018-2020 (raw data),
290 https://dataplatform.knmi.nl/dataset/windlidar-cabauw-zephir300m-zx973-1s-1 (accessed: 06.01.2023), 2023a.

KNMI: Wind - lidar data from ZephIR 300M (unit ZP738) during Cabauw campaign 2018-2020 (raw data), https://dataplatform.knmi.nl/dataset/windlidar-cabauw-zephir300m-zp738-1s-1 (accessed: 06.01.2023), 2023b.

KNMI: Wind - lidar wind profiles measured at North Sea wind farm TenneT platforms 1 second raw data, https://dataplatform.knmi.nl/dataset/windlidar-nz-wp-platform-1s-1 (accessed: 05.01.2023), 2023c.

295 Lampert, A., Bärfuss, K., Platis, A., Siedersleben, S., Djath, B., Cañadillas, B., Hunger, R., Hankers, R., Bitter, M., Feuerle, T., et al.: In situ airborne measurements of atmospheric and sea surface parameters related to offshore wind parks in the German Bight, Earth System Science Data, 12, 935–946, 2020.

Lobo, B. A., Özçakmak, Ö. S., Madsen, H. A., Schaffarczyk, A. P., Breuer, M., and Sørensen, N. N.: On the laminar–turbulent transition mechanism on megawatt wind turbine blades operating in atmospheric flow, Wind Energy Science, 8, 303–326, 2023.

300 Mandelbrot, B. B.: The fractal geometry of nature, vol. 1, WH freeman New York, 1982.

Milan, P., Wächter, M., and Peinke, J.: Turbulent character of wind energy, Physical review letters, 110, 138 701, 2013.

Sreenivasan, K. and Meneveau, C.: The fractal facets of turbulence, Journal of Fluid Mechanics, 173, 357–386, 1986.

Taylor, G. I.: The spectrum of turbulence, Proceedings of the Royal Society of London. Series A-Mathematical and Physical Sciences, 164, 476–490, 1938.

305 Xu, C., Long, Y., and Wang, J.: Entrainment mechanism of turbulent synthetic jet flow, Journal of Fluid Mechanics, 958, A31, 2023.